Article

Not peer-reviewed version

Correlative Multi-scale Characterization of Nanoparticles Using Transmission Electron Microscopy

Stefan Neumann and David Rafaja *

Posted Date: 5 September 2024

doi: 10.20944/preprints202409.0256.v1

Keywords: Transmission electron microscopy; crystal structure defects; semi-automatic image segmentation; kernel density estimator; gold nanoparticles; gold nanorods; multi-core iron oxide nanoparticles

 doi:10.20944/preprints202409.0256.v1

Article

Correlative Multi-Scale Characterization of Nanoparticles Using Transmission Electron Microscopy

Stefan Neumann and David Rafaja *

Institute of Materials Science, Technische Universität Bergakademie Freiberg, Germany
* Correspondence: rafaja@iww.tu-freiberg.de

Abstract: Chemical and physical properties of nanoparticles (NPs) are strongly influenced not only by the crystal structure of the respective material including crystal structure defects, but also by the NP size and shape. Contemporary transmission electron microscopy (TEM) is capable of describing all of these NP characteristics, however typically with a different statistical relevance. While the size and shape of NPs are frequently determined on a large ensemble of NPs and thus with good statistics, the characteristics on the atomic scale are usually quantified for a small number of individual NPs and thus with a low statistical relevance. In this contribution, we present a TEM-based characterization technique, which is capable of determining relevant characteristics of NPs in a scale-bridging way – from the crystal structure and crystal structure defects up to the NP size and morphology – with a sufficient statistical relevance. This technique is based on a correlative multi-scale TEM approach that combines information on atomic scale obtained from the high-resolution imaging with the results of the low-resolution imaging assisted by a semi-automatic segmentation routine. The capability of the technique is illustrated on several examples including Au NPs having different shape, Au nanorods having different facet configurations and multi-core iron oxide nanoparticles having a hierarchical structure.

Keywords: transmission electron microscopy; crystal structure defects; semi-automatic image segmentation; kernel density estimator; gold nanoparticles; gold nanorods; multi-core iron oxide nanoparticles

1. Introduction

Nanoparticles (NPs) having the size between 1 nm and 100 nm possess a huge potential for applications in various technological fields, *e.g.*, in electronics and optoelectronics [1,2], in catalysis [3,4] or in biomedicine [5,6]. Their unique properties, such as the localized surface plasmon resonance (LSPR) in noble metal NPs [7], the superparamagnetism in metal alloy and metal oxide NPs [8] or the quantum confinement in semiconductor quantum dots [9], are facilitated by the small size of the NPs, as these properties are not observed in the bulk counterparts of the same material. The chemical and physical properties of NPs are basically controlled by their chemical composition [10] and crystal structure [11], and influenced by the presence of crystal structure defects [12] like in bulk materials. Additionally, the properties of NPs are strongly affected by their size [13], shape [14] and surface morphology [15]. During the last decades, great efforts have been made to develop reliable procedures for production of NPs with specific structure and microstructure characteristics and thus with desired and well-defined materials properties [3,8,10,12,15–31].

In order to be able to correlate the physical and chemical properties of NPs with their structure and microstructure characteristics reliably, scale-bridging approaches for structure analysis must be developed that allow the structure and microstructure of NPs to be quantified in-depth on different length scales and with sufficient statistical relevance. Integral methods, such as UV-Vis spectroscopy [32], dynamic light scattering [33], small-angle X-ray scattering and wide-angle X-ray diffraction [34], have been proven to be powerful tools enabling statistically relevant studies of morphological and

 doi:10.20944/preprints202409.0256.v1

structural characteristics of different kinds of NPs. However, the information, which is obtained using these integral methods, is *a priori* averaged over the whole ensemble of the NPs under study. Thus, the morphological and structural characteristics cannot be assigned to individual NPs. Frequently, the integral techniques do not yield even the distribution function for the respective characteristic, which tremendously complicates the determination of correlations between two or more characteristics or properties.

The characterization of individual NPs is only possible using experimental techniques that have a sufficient lateral resolution. In this context, the combination of three-dimensional X-ray micro- or nanotomography with two-dimensional scanning electron microscopy coupled with energy dispersive X-ray spectroscopy has been shown to be a suitable approach for the characterization of particles having the size ranging between several hundreds of micrometers and approximately one micrometer [35–37]. NPs with the size below 100 nm, however, can be investigated in sufficient depth by the transmission electron microscopy (TEM) only. TEM, in particular in conjunction with the high-resolution imaging (HRTEM), offers an excellent lateral resolution. However, it suffers from a typically low statistical reliability, which is caused by a limited number of the NPs under study.

This contribution illustrates the capability of a TEM-based correlative multi-scale approach that is able to determine the relevant characteristics of NPs on atomic and sub-micrometer scale in a sufficiently detailed and statistically relevant manner. The information on the atomic scale is obtained from the HRTEM images, and from their fast Fourier transform (FFT) and geometric phase analysis (GPA) [38,39]. The information on the sub-micrometer scale is obtained from a semi-automatic segmentation and statistical evaluation of low-resolution TEM images that were recorded by a high-angle annular dark-field detector. The applicability of the correlative multi-scale approach is demonstrated on various examples: on the classification of the Au NPs with different morphology, on the statistical determination of the facet configurations in Au nanorods (NRs) and on the determination of the hierarchical structure of multi-core iron oxide nanoflowers (IONFs).

2. Materials and Methods

2.1. Nanoparticle Synthesis

The Au nanoparticles (Au NPs) were synthesized by adding an aqueous solution containing trisodium citrate and tannic acid to an aqueous solution containing hydrogen tetrachloroaurate(III) trihydrate. The synthesis route was described in detail in Refs. [16,22,40,41]. The temperature of the synthesis was 60 °C. The Au nanorods (Au NRs) were synthesized using the procedure invented by Ye *et al.* [24]. The seed solution was prepared by mixing $HAuCl_4$ with cetyltrimethylammonium bromide (CTAB) solution. Freshly prepared $NaBH_4$ was injected to the Au(III)-CTAB solution under stirring. The growth solution was prepared by dissolving cetyltrimethylammonium chloride (CTAC) and sodium oleate (NaOL) in warm water ($\sim$ 50 °C). After cooling down to 30 °C, a $AgNO_3$ solution was added. After 150 min of stirring, HCl was introduced. After another 15 min of stirring, ascorbic acid was added and the solution was continuously stirred. Finally, the seed solution was injected into the growth solution, the resultant mixture was stirred for 30 s and left at 30 °C for 12 h. The as-synthesized Au NRs were separated by centrifugation and then transferred to deionized water. In a final step, the Au NRs stabilized with 11-mercaptoundecanoic acid were obtained by a ligand exchange. Further details on the synthesis of the Au NRs can be found in Refs. [24,40,42]. The multi-core iron oxide nanoflowers (IONFs) investigated in this study were commercially available dextran-coated maghemite nanoparticles (synomag-D, micromod Partikeltechnologie GmbH, Germany) [43], which were synthesized by a polyol method adapted from Lartigue *et al.* [44]. Details on the synthesis of the IONFs can be found in Ref. [27].

 doi:10.20944/preprints202409.0256.v1

2.2. Nanoparticle Characterization

For the scale-bridging analysis of the crystal structure and morphology of the NPs, a combination of the high-resolution transmission electron microscopy (HRTEM) and the 'low-resolution' high-angle annular dark-field scanning transmission electron microscopy (HAADF-STEM) was utilized. The HRTEM images revealed information about the size and shape of individual NPs that was complemented by the crystallographic orientations of the NP facets, by the kind of the crystal structure defects and by the related local displacement fields, which were obtained from the fast Fourier transform (FFT/HRTEM) and from the geometric phase analysis (GPA) [38,39] of the HRTEM micrographs. The HAADF-STEM images were processed by a semi-automatic segmentation routine [40] in order to get a statistically relevant information about the distribution of the NP size and shape, which was correlated with the corresponding characteristics determined using HRTEM. As the STEM images were recorded by a HAADF detector, they contained a three-dimensional information about the particle shape.

All TEM experiments were carried out in a transmission electron microscope (JEM 2200FS from JEOL Ltd., Japan), which was equipped with a field emission gun operating at 200 kV, with a CESCOR probe aberration corrector (CEOS GmbH, Germany), with an ultra-high resolution objective lens ($C_S = 0.5$ mm), with an in-column energy filter (Ω-filter), and with a 2K × 2K CCD camera (Gatan, Inc., USA). The Ω-filter was used to filter inelastically scattered electrons and thus to improve the quality of the HRTEM images. The HAADF-STEM images were recorded in scanning mode by an upper HAADF detector (EM-24630 UHADF, JEOL Ltd., Japan). For the TEM analyses, the NPs were suspended in a suitable solvent and sprayed on a standard copper TEM grid that was covered with an amorphous carbon film.

3. Results and Discussion

3.1. Classification of Au Nanoplates and Multiply Twinned Au Nanoparticles

The Au NPs possess exceptional optical properties, which are caused by the localized surface plasmon resonance (LSPR) effect [45,46]. The LSPR effect is a result of the collective resonant oscillations of conduction electrons, which are excited by the electromagnetic field of the incident light [7,47]. An important consequence of the LSPR effect is the appearance of optical extinction at a specific frequency that depends mainly on the size [48] and shape [49] of the Au NPs, and that is affected by the kind and density of the crystal structure defects [12]. The Au NPs can grow as small faceted single crystals having truncated octahedral (TOh) shape [21], as multiply twinned particles (MTPs) [50] with either icosahedral (Ih) or decahedral (Dh) shape, or as nanoplates (NPLs) [17]. The Au NPs contain typically planar defects that are mainly stacking faults (SFs) and twins (TWs). The shape of Au NPs depends usually on the conditions of the Au NP synthesis [21]. However, as the transition between the individual types of the Au NPs is smooth, Au NPs with different properties can occur within the same sample [25]. Therefore, an experimental technique for statistically reliable classification of the Au NPs is required, in particular if the structural characteristics of the NPs are to be correlated with their properties. This section illustrates, how the NP shape can be correlated with the kind of the crystal structure defects and how the combination of HRTEM and HAADF-STEM improves the statistical quality of the Au NP classification.

HRTEM images of individual Au NPs (Figure 1) reveal a coexistence of NPLs and MTPs. While NPLs appear as truncated triangles (upper panels in Figures 1a and 1b) with almost perfect crystal structure, MTPs look like disks with a high density of planar defects (upper panels in Figure 1c and 1d). According to FFT/HRTEM (lower panels in Figures 1a and 1b), almost all Au NPLs possess a $\langle 111 \rangle$ orientation along the direction of the primary electron beam. The truncated triangles are terminated by the lattice planes $\langle 211 \rangle$. The diffraction spots highlighted by dotted circles that resemble the reflections $\frac{1}{3}\{422\}$ are produced by the stacking faults that are located on the lattice planes $\{111\}$, which are

 doi:10.20944/preprints202409.0256.v1

perpendicular to the direction of the primary electron beam. Such SFs are not visible directly in the HRTEM images, but they produce truncation rods $\{111\}$, which intersect the Ewald sphere at the reciprocal space vector having the size of

$$|\vec{q}_{xy}\{111\}| = 2\pi/d_{111} \cdot \sin\varphi = 2\pi\sqrt{3}/a \cdot \sin\varphi, \quad (1)$$

where $d_{111} = a/\sqrt{3}$ is the interplanar spacing of the lattice planes $\{111\}$, $a = 4.078$Å the lattice parameter of Au and $\varphi = 70.53°$ or $109.47°$ the angle between the faulted lattice planes (111) and the crystallographically equivalent lattice planes $\{111\}$. As $\sin\varphi \approx \sqrt{8}/3$ for both φ angles, the q_{xy} positions of the truncation rods $\bar{1}11$, $1\bar{1}1$, $11\bar{1}$, $\bar{1}\bar{1}1$, $1\bar{1}\bar{1}$ and $\bar{1}1\bar{1}$ are almost equal to one third of the q_{xy} positions of the reciprocal lattice points $\bar{4}22$, $2\bar{4}2$, $22\bar{4}$, $\bar{2}\bar{2}4$, $4\bar{2}\bar{2}$ and $\bar{2}4\bar{2}$, *i.e.*,

$$|\vec{q}_{xy}\{422\}|/3 = 2\pi/\left(3d_{422}\right) = 2\pi\sqrt{3}/a \cdot \sqrt{8}/3. \quad (2)$$

In the HRTEM images of multiply twinned particles (Figures 1c and 1d), the stacking faults are visible directly, because the normal directions to the faulted lattice planes are not perpendicular to the diffraction vector. The projected form of the particles appears almost circular for both MTPs classes, *i.e.*, for Dh shaped (Figure 1c) and Ih shaped (Figure 1d) MTPs. Still, these particle shapes can be distinguished by means of FFT/HRTEM. The FFT/HRTEM of the Dh MTPs shows a pattern with a 'five-fold symmetry' consisting of ten 111 diffraction spots (marked by solid circles in Figure 1c) and ten 200 diffraction spots (marked by solid boxes in Figure 1c) that have approximately equidistant azimuthal positions. The FFT/HRTEM patterns of the Ih MTPs contain additional diffraction spots (marked by dashed circles in Figure 1d), which are caused by the Moiré pattern effect [51].

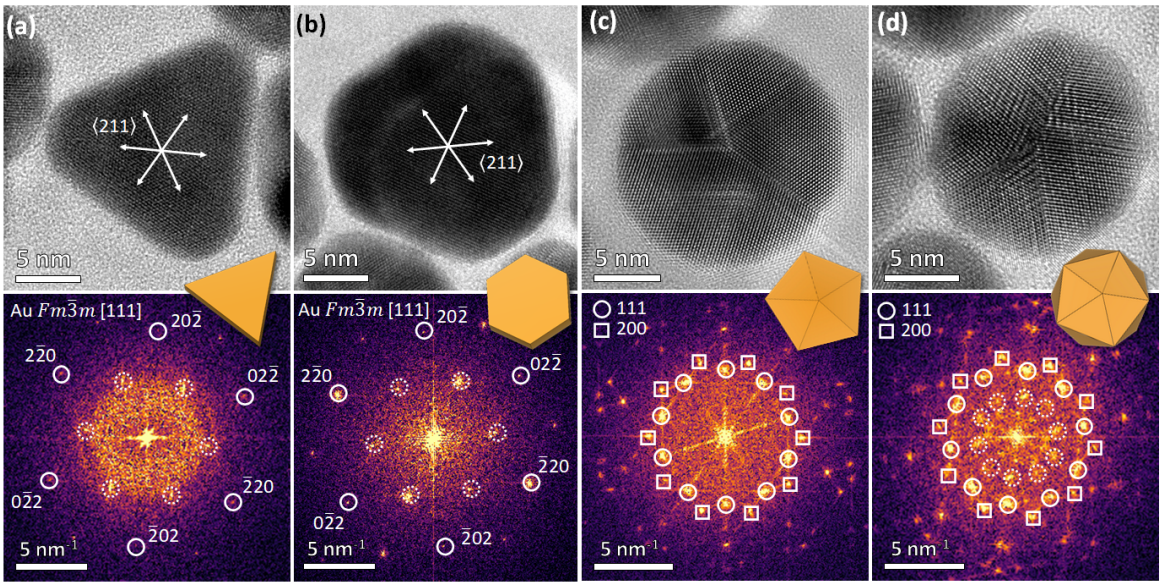

Figure 1. HRTEM images (upper panels) of typical Au NPs and their fast Fourier transforms (FFTs, bottom panels). The schematic shapes of the NPs are depicted between the panels. (a) Au nanoplates (NPLs) with triangular projected shape, (b) Au NPLs with hexagonal projected shape, (c) multiply twinned particles (MTPs) with decahedral (Dh) shape and (d) MTPs with icosahedral (Ih) shape.

As illustrated above, several kinds of Au NPs, *e.g.*, 'flat triangular' NPLs with different degree of truncation and 'spherical' MTPs having the Dh or Ih shapes, can be differentiated using the HRTEM imaging. Using FFT/HRTEM, the NP edges can be assigned to the crystallographic directions and the NP shape can be correlated with the kind and orientation of the planar defects [18,40]. However, these techniques operating on the atomic scale are not suitable to reveal a statistically relevant information about the individual NP fractions. Therefore, for statistical reasons, HRTEM was combined with a

 doi:10.20944/preprints202409.0256.v1

'low-magnification' HAADF-STEM imaging, which is indeed not able to visualize the crystal structure defects directly, *i.e.*, on the atomic scale, but it can recognize different NPs according to their projected shape. Furthermore, as the HAADF-STEM signal stems from the Rutherford scattering of the primary beam electrons on the atomic nuclei within the sample, the HAADF-STEM intensity measured on Au NPs depends mainly on the NP thickness [52]. As the Au NPs contain only a single element, the dependence of the HAADF-STEM intensity on the atomic number does not play any role. Consequently, the HAADF-STEM signal from Au NPs can be used to determine their 3D form.

The information about the NP thickness and especially the information about the thickness variation within individual NPs can help to classify the Au NPs into the 'flat triangular' NPLs and 'spherical' MTPs. For a quantitative classification of the NPs, the relative variance of the HAADF-STEM intensity within individual NPs (Figure 2a) was used:

$$\widetilde{I} = \frac{\sigma_I}{\mu_I} \tag{3}$$

The mean HAADF-STEM intensity,

$$\mu_I = \frac{1}{N}\sum_{i=1}^{N} I_i^{\mathrm{HAADF}}, \tag{4}$$

and its variance,

$$\sigma_I = \sqrt{\frac{1}{N-1}\sum_{i=1}^{N}(I_i^{\mathrm{HAADF}} - \mu_I)^2}, \tag{5}$$

were calculated from the HAADF-STEM intensity values (I_i^{HAADF}) that were measured within individual NPs. N in equations (4) and (5) denotes the number of pixels within the respective NP.

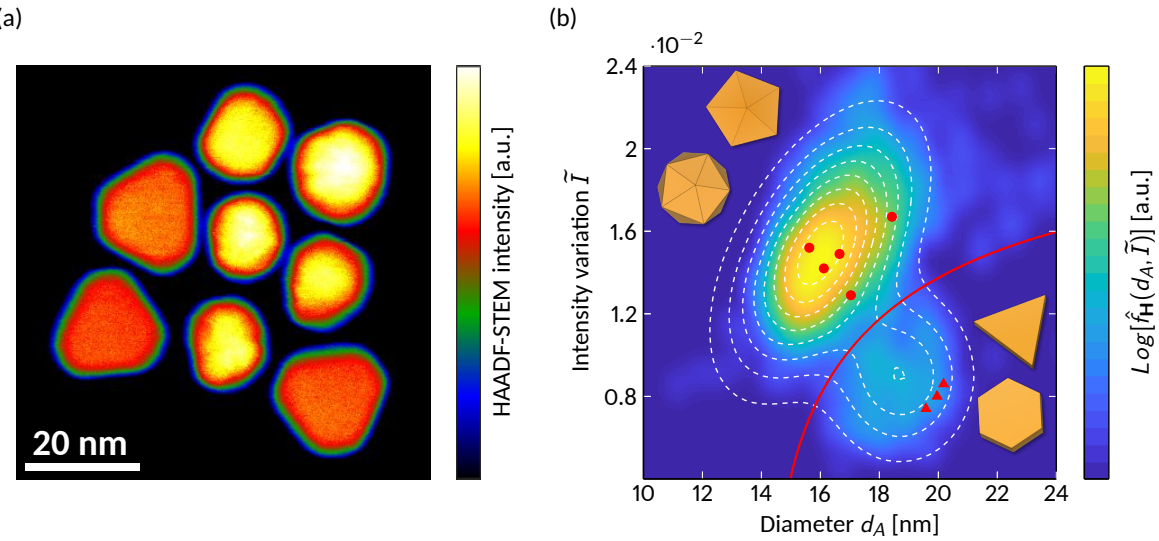

Figure 2. (a) HAADF-STEM intensity distribution measured for Au NPLs (particles with almost constant intensity) and MTPs (particles with a strong intensity variation). (b) Correlation between the area-equivalent diameter (d_A, Equation (6)) and the variation of the HAADF-STEM intensity ($\widetilde{I}$, Equation (3)) as obtained for an ensemble of approx. 2,700 Au NPs. The colors represent the values of the bivariate kernel density estimator $\hat{f}_{\mathbf{H}}(d_A, \widetilde{I})$ from Equation (7). Red circles and triangles mark the positions of the MTPs and NPLs depicted in panel (a). The white dashed lines are the isolines of a sum of two 2D Gaussian functions that were fitted to $\hat{f}_{\mathbf{H}}(d_A, \widetilde{I})$. The red line marks the transition between MTPs and NPLs that was determined using Equation (8).

 doi:10.20944/preprints202409.0256.v1

In order to improve the reliability of the classification procedure, $\widetilde{I}$ from Equation (3) was correlated with the area-equivalent diameter of the respective NP that was calculated from the projected area A:

$$d_A = \sqrt{\frac{4A}{\pi}}, \tag{6}$$

The area itself was determined from the number of pixels, which were assigned to the respective NP. In Figure 2b, the correlation between $\widetilde{I}$ and d_A is visualized using two bivariate density estimators [53]

$$\hat{f}_{\mathbf{H}}(d_A, \widetilde{I}) = \frac{1}{M h_{d_A} h_{\widetilde{I}}} \sum_{j=1}^{M} K\left(\frac{d_A - d_{A,j}}{h_{d_A}}, \frac{\widetilde{I} - \widetilde{I}_j}{h_{\widetilde{I}}}\right) \tag{7}$$

that are based on the Gaussian kernel functions K. $d_{A,j}$ and $\widetilde{I}_j$ are the characteristics of the j^{th} NP, and h_{d_A} and $h_{\widetilde{I}}$ are the bandwidths of the kernel function that were determined according to Scott's rule [54].

This classification procedure allows NPLs to be distinguished from MTPs, and the respective NP fraction to be determined. It can be seen from Figures 2a and 2b that NPLs show a smaller variation of the HAADF-STEM intensity and that are typically larger than MTPs. The transition between NPLs and MTPs (red line in Figure 2b) was determined using the indicator function

$$\mathbf{1}_{\text{MTP}}(d_A, \widetilde{I}) = \begin{cases} 1 & \text{if} \quad f_{\text{MTP}}(d_A, \widetilde{I}) \geq f_{\text{NPL}}(d_A, \widetilde{I}) \\ 0 & \text{if} \quad f_{\text{MTP}}(d_A, \widetilde{I}) < f_{\text{NPL}}(d_A, \widetilde{I}) \end{cases} \tag{8}$$

For MTPs, $\mathbf{1}_{\text{MTP}}(d_A, \widetilde{I})$ is equal to unity, while for NPLs, $\mathbf{1}_{\text{MTP}}(d_A, \widetilde{I}) = 0$. The number of MTPs was obtained from the 'weighted' integration of the function $\hat{f}_{\mathbf{H}}(d_A, \widetilde{I})$,

$$N_{\text{MTP}} = \iint \hat{f}_{\mathbf{H}}(d_A, \widetilde{I}) \mathbf{1}_{\text{MTP}}(d_A, \widetilde{I}) \mathrm{d}d_A \mathrm{d}\widetilde{I} \tag{9}$$

The MTP fraction was calculated as

$$\mu_{\text{MTP}} = \frac{N_{\text{MTP}}}{N_{\text{total}}}, \tag{10}$$

where N_{total} is the total number of NPs. The fraction of NPLs is equal to $\mu_{\text{NPL}} = 1 - \mu_{\text{MTP}}$. The statistical analysis carried out with $\sim$ 2,700 Au NPs revealed that the sample under study contains approx. 90% of MTPs and about 10% of NPLs.

In conjunction with the results of HRTEM and FFT/HRTEM, the result of HAADF-STEM provides an important insight into the kinetics of the growth process of Au NPs, because the kind and the density of planar defects and consequently the morphology of the Au NPs are controlled by the reaction rate during the synthesis [20,25]. At a sufficiently high reaction rate, defect-free NPs with truncated octahedral (TOh) shape develop [21,55]. Reduction of the reaction rate leads to the stabilization of multiply twinned particles (MTPs) [21,50,56]. A further reduction of the reaction rate promotes formation of NPs with plate-like morphology that contain a high density of planar defects preferentially on a single system of the (111) lattice planes [17,57,58]. The absence of TOh NPs and the presence of $\sim$ 90% MTPs and $\sim$ 10% NPLs in the Au NPs under study indicate that the reaction conditions were moderate. However, the reduction rate was not sufficiently high to produce exclusively MTPs.

Although the statistical HAADF-STEM analysis of the Au NPs that is supported by the FFT/HRTEM investigation of few selected NPs reveals a valuable information about the kind and distribution of the planar defects, and although this technique provides an important insight into the growth conditions, further details, for instance about the stacking fault density, can only be obtained using the analytical methods operating on the atomic scale.

 doi:10.20944/preprints202409.0256.v1

3.2. Classification of Differently Faceted Au Nanorods

Similarly to Au NPs, the Au nanorods (Au NRs) show also unique plasmonic properties [59]. However, in contrast to Au NPs that possess typically one LSPR band, Au NRs produce two LSPR bands, which correspond to the plasmonic oscillations along their short and long axes [46]. The optical properties of Au NRs depend mainly on their size and aspect ratio. For applications in catalysis, the crystallographic orientation of the Au NRs facets plays a crucial role. Zhang *et al.* [15] have shown that Au NRs terminated by high-index facets possess a higher catalytic activity than Au NRs with low-index facets.

The example from Section 3.1 illustrated the capability of the statistical classification of Au NPs by HAADF-STEM supported by HRTEM and FFT/HRTEM. However, in that example the information obtained from HRTEM was not fully linked with the information obtained from HAADF-STEM, as the exact projected NP shape was not considered when analyzing the HAADF-STEM images. The NPLs with triangular (less truncated) and hexagonal (heavily truncated) form or the MTPs with decahedral and icosahedral shape were not classified separately (Figure 2). Thus, the densities of planar defects were not determined statistically. The example presented in this section illustrates, how Au NRs can be classified into four categories, when their 3D shape is used.

The in-depth characterization of the Au NRs on the atomic scale was carried out using HRTEM and FFT/HRTEM on several tens of nanorods. The HRTEM images taken on reclined Au NRs (Figure 3a) confirmed that they are single-crystalline, possess the *fcc* structure, and are defect-free and elongated along one of the crystallographic directions $\langle 001 \rangle$, as it was already reported by Zhang *et al.* [15] and Ye *et al.* [24]. The caps of the Au NRs are usually formed by the high-index facets $\{013\}$. The angle between these facets is 143°, as it is visible in the HRTEM image from Figure 3a, where the facets (013) and $(0\bar{1}3)$ are highlighted in red. The cross sections of the Au NRs (Figure 3b) are typically terminated by the high-index facets $\{013\}$ [24], but in some cases also the low-index facets of the $\{100\}$ and $\{110\}$ types were found. This result was confirmed by the presence of differently oriented reclined NRs (s. Figure 3d).

According to Figure 3c, the angles between the high-index facets $\{013\}$ are either 143.1°, *e.g.*, between $(\bar{3}10)$ and $(\bar{3}\bar{1}0)$, or 126.9° like for $(\bar{3}\bar{1}0)$ and $(\bar{1}\bar{3}0)$. The angles between the corresponding crystallographic directions $(\bar{3}10)$, and $(\bar{3}\bar{1}0)$ and $(\bar{1}\bar{3}0)$ are 36.9° and 53.1°, respectively. The high-index facets are believed to develop in the final stage of a seed-mediated Au NR synthesis, as they smooth the sides of the NRs by removing the edges between the previous side facets $\{100\}$ and $\{110\}$ [28]. In general, a high number of crystallographically equivalent lattice planes distributed along a specific zone axis ($\{hk0\}$ in Figure 3c) smooths the kinks between the neighboring facets. From the crystallographic point of view, the number of crystallographically equivalent lattice planes increases with increasing number of non-equal h, k and l values within the Miller index hkl. Thus, a combination of the high-index and low-index facets also facilitates the smoothing of the NR surface. From the atomistic point of view, however, the high-angle facets produce steps on the surface of the NRs.

 doi:10.20944/preprints202409.0256.v1

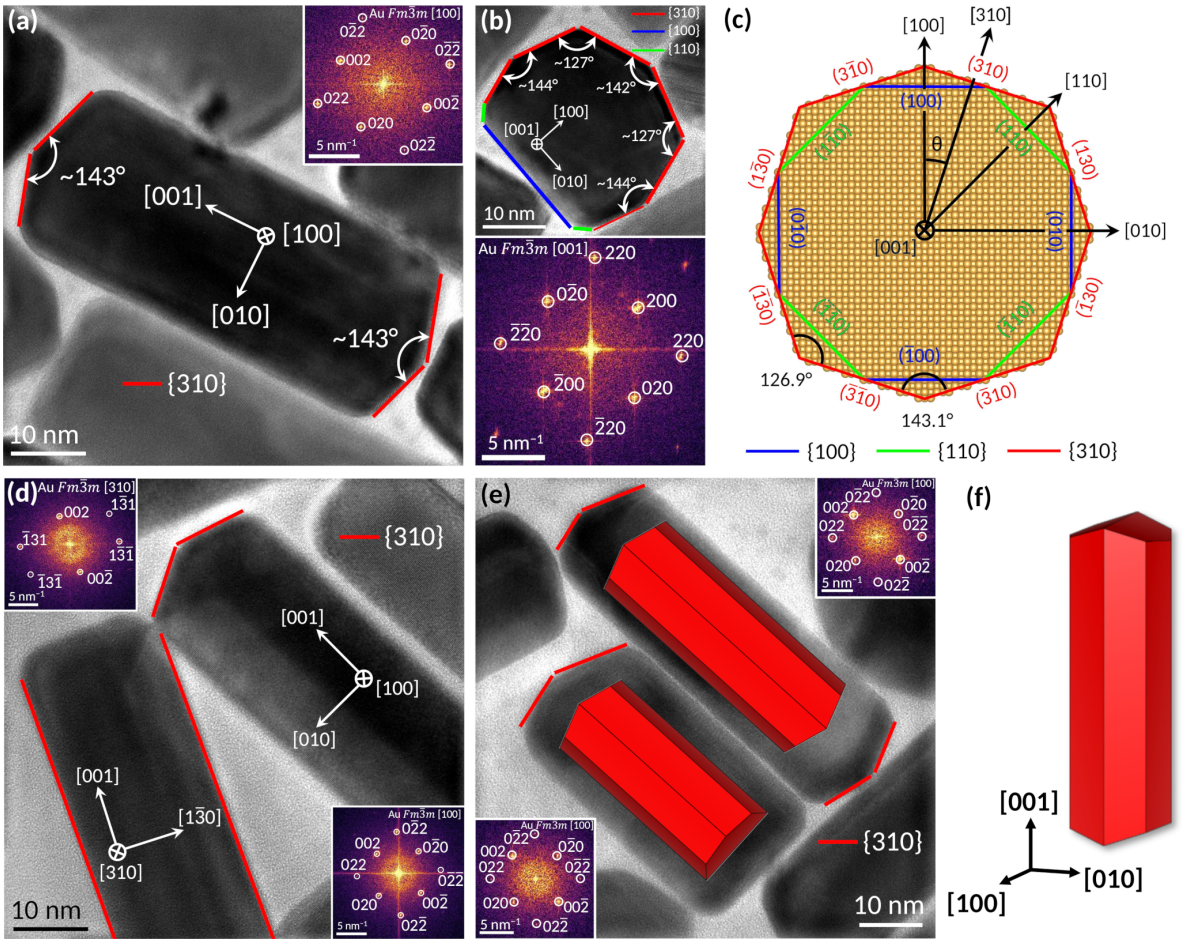

Figure 3. HRTEM images of Au NRs oriented with their growth direction [001] perpendicular (a) and parallel (b) to the direction of the primary electron beam. (c) Cross section of a NR illustrating the orientations of low-index {100}, {110}, and high-index {310} facets. (d) Au NRs viewed along the zone axes [310] and [100] that represent a completely and an incompletely {310}-faceted cross section, respectively. (e) Au NRs with symmetric and asymmetric caps. The insets in panels (a), (b), (d) and (e) show the FFTs of the respective HRTEM image. (f) Geometrical model of an Au NR that is completely terminated by high-index {310} facets.

For subsequent statistical analysis using HAADF-STEM, the Au NRs were divided into four categories of 'faceted cylinders' capped by differently oriented lattice planes. The cross-sections of the cylinders are either *complete* or *incomplete*. The NRs with *complete* cross-sections are terminated by the high-index facets {310} only. The NRs with *incomplete* cross-section possess one low-index facet, typically of the type {100} (Figure 3b). The caps of the NRs are either *symmetric* or *asymmetric*. The NRs with *symmetric* caps are terminated on both ends by the same facet type, *i.e.*, $(0, \pm 1, 3)$ and $(0, \pm 1, \bar{3})$ or $(\pm 1, 0, 3)$ and $(\pm 1, 0, \bar{3})$. The NRs with *asymmetric* caps are terminated by facets, which are mutually rotated by 90° at the respective end, *i.e.*, $(0, \pm 1, 3)$ and $(\pm 1, 0, \bar{3})$ or $(\pm 1, 0, 3)$ and $(0, \pm 1, \bar{3})$.

Since the majority of NRs lies horizontally on the TEM grid, the NR symmetry is typically visible directly from the 2D HAADF-STEM projection (Figure 4a). In the semi-automatic segmentation and classification routine [40], the ratio of the NR diameters measured at the top and at the bottom of the NRs (Figure 4b),

$$\delta_T = \min\left(\frac{D_{\text{Top}}}{D_{\text{Bottom}}}, \frac{D_{\text{Bottom}}}{D_{\text{Top}}}\right), \tag{11}$$

Preprints.org (www.preprints.org) | NOT PEER-REVIEWED | Posted: 5 September 2024 doi:10.20944/preprints202409.0256.v1

is employed as the parameter quantifying the degree of the NRs symmetry. For NRs with *symmetric* caps, $\delta_T \approx 1$. For NRs with *asymmetric* caps, $\delta_T \ll 1$ (Figure 5). The completeness of the NR cross-sections is quantified by

$$\delta_C = \frac{D_{CS}}{D}, \tag{12}$$

where D_{CS} is the width of the plateau in the HAADF-STEM intensity profile measured across the NR (Figure 4c) and D the width of the whole NR. For *complete* NRs, $\delta_C = 1/\left[1 + \sin(2\theta) + \cos(2\theta)\right] \approx 0.42$ (cf. Figure 5), where θ is the angle between the directions [310] and [100], *i.e.*, 18.4°. For *incomplete* NRs, δ_C is less than 0.42. In the example from Figure 4c showing the presence of a single {100} facet, δ_C would converge to zero.

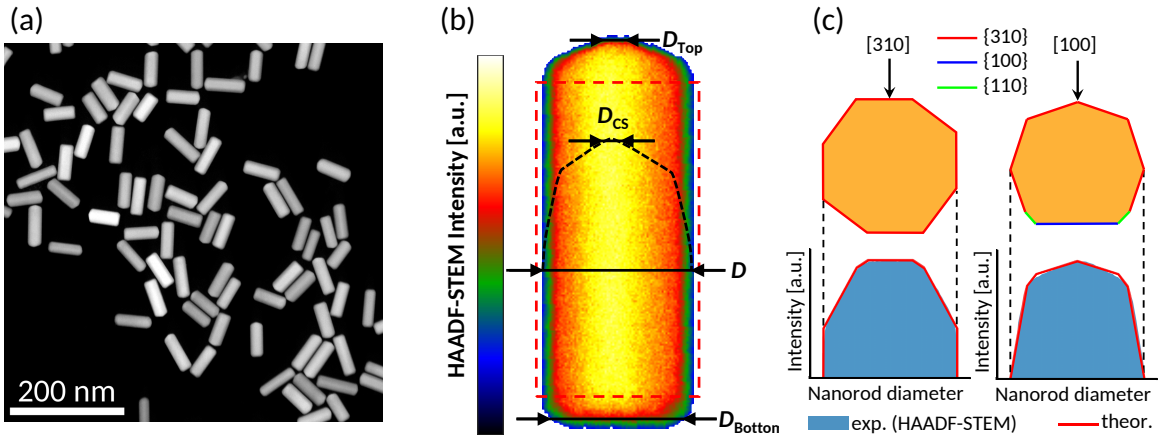

Figure 4. (a) Example of a low-magnification HAADF-STEM image of Au NRs. (b) Schematic shape of a single Au NR approximated by a 'faceted cylinder' with differently oriented polygonal caps; the HAADF-STEM intensity is proportional to the thickness of the NR along the direction of the primary beam. (c) Difference in the HAADF-STEM intensity profiles measured along the D direction (see panel (b)) in the NRs with *complete* (left) and *incomplete* (right) cross-sections. The relative width of the intensity plateau (δ_C from Equation (12)) is used as a measure of the NR completeness. The ratio between the NR diameter obtained from the HAADF-STEM intensity measured at the top and at the bottom caps of the NR (δ_T from Equation (11)) is used as a measure of the symmetry of the NR caps (tips).

Preprints.org (www.preprints.org) | NOT PEER-REVIEWED | Posted: 5 September 2024 doi:10.20944/preprints202409.0256.v1

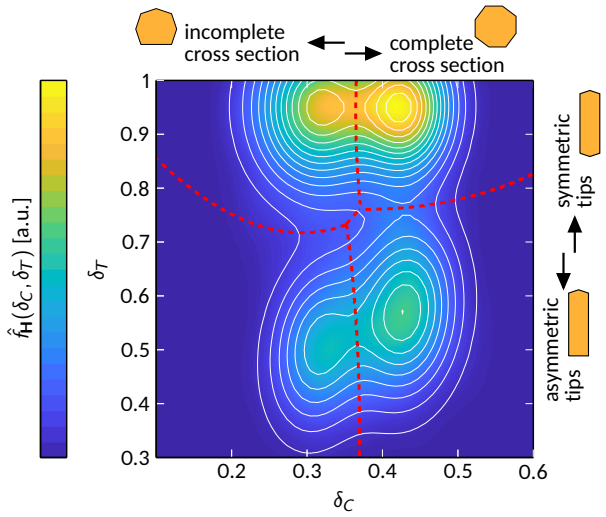

Figure 5. Two-dimensional distribution density of the parameters δ_T and δ_C plotted in terms of their bivariate kernel density estimator, $\hat{f}_{\mathbf{H}}(\delta_C, \delta_T)$. The white lines represent isolines of the sum of four 2D Gaussian functions fitted to the four maxima of $\hat{f}_{\mathbf{H}}(\delta_C, \delta_T)$. The red dashed lines mark the boundaries between the NRs with the respective facet configuration that were determined according to Equation (15).

In Figure 5, the two-dimensional distribution density of the parameters δ_T and δ_C is depicted in terms of the bivariate kernel density estimator, $\hat{f}_{\mathbf{H}}(\delta_C, \delta_T)$, which was determined in analogy to Equation (7). Individual maxima of $\hat{f}_{\mathbf{H}}(\delta_C, \delta_T)$, *i.e.*, $f_i^s(\delta_C, \delta_T)$, $f_c^s(\delta_C, \delta_T)$, $f_i^a(\delta_C, \delta_T)$ and $f_c^a(\delta_C, \delta_T)$, were fitted by 2D Gaussian functions and assigned to NRs with *incomplete* cross sections and *symmetric* caps, to NRs with *complete* cross sections and *symmetric* caps, to NRs with *incomplete* cross sections and *asymmetric* caps, and to NRs with *complete* cross sections and *asymmetric* caps, respectively.

The fitted functions $f_i^s(\delta_C, \delta_T)$, $f_c^s(\delta_C, \delta_T)$, $f_i^a(\delta_C, \delta_T)$ and $f_c^a(\delta_C, \delta_T)$ were used to identify the boundaries between the NR categories (red lines in Figure 5) and to determine the amounts of NRs having the respective facet configuration. The boundaries between the NR categories obey the relationships

$$\begin{aligned} f_i^s(\delta_C, \delta_T) = f_c^s(\delta_C, \delta_T)\,; \;\; f_i^s(\delta_C, \delta_T) = f_i^a(\delta_C, \delta_T) \\ f_c^s(\delta_C, \delta_T) = f_c^a(\delta_C, \delta_T)\,; \;\; f_i^a(\delta_C, \delta_T) = f_c^a(\delta_C, \delta_T) \end{aligned} \tag{13}$$

The amount of NRs having the particular facet configuration follows from the integration of the bivariate kernel density estimator $\hat{f}_{\mathbf{H}}(\delta_C, \delta_T)$ over the respective (δ_C, δ_T) region. For example, the amount of NRs with complete cross sections and symmetric caps is equal to

$$\mu_c^s = \frac{N_c^s}{N} = \int_0^1 \int_0^1 \hat{f}_{\mathbf{H}}(\delta_C, \delta_T) \mathbf{1}_c^s(\delta_C, \delta_T) \mathrm{d}\delta_C \mathrm{d}\delta_T, \tag{14}$$

where

$$\mathbf{1}_c^s(\delta_C, \delta_T) = \begin{cases} 1, & f_c^s(\delta_C, \delta_T) \geq f_c^a(\delta_C, \delta_T), f_i^s(\delta_C, \delta_T), f_i^a(\delta_C, \delta_T) \\ 0, & f_c^s(\delta_C, \delta_T) < f_c^a(\delta_C, \delta_T), f_i^s(\delta_C, \delta_T), f_i^a(\delta_C, \delta_T) \end{cases} \tag{15}$$

is the indicator function for NRs with the particular facet configuration. The amounts of NRs with other configurations of the facets are calculated analogously.

The statistical evaluation of the HAADF-STEM measurements summarized in Figure 5 revealed that about 33% of the Au NRs have *complete* cross sections and *symmetric* caps. According to HRTEM, these NRs are fully terminated by the high-index facets $\{310\}$. Approximately 24% of the Au NRs still

 doi:10.20944/preprints202409.0256.v1

possess *complete* cross sections, but have *asymmetric* caps. In total, the cross sections of $\sim$ 43% Au NRs were *incomplete*. Approximately 28% of them have *symmetric* and about 15% *asymmetric* caps. In this context, it should be noted that the completeness of the cross sections quantified using Equation(12) is primarily an indicator of the presence or absence of parallel opposite facets oriented perpendicular to the direction of the primary electron beam (Figure 4c). Nevertheless, assuming an equal growth rate in the crystallographically equivalent directions $\{310\}$, the second maxima of δ_C appearing at ~ 0.34 (Figure 5) can only be explained by the presence of other facets than $\{310\}$ that are perpendicular to the primary beam. Still, the non-parallel opposite facets like in Figure 3b, whose presence would lead to extremely low δ_C values, are rare.

The stabilization of specific facets in noble metal NPs is generally attributed to the presence of certain surface capping agents [31] and structure-directing ions [23,60,61]. The formation of high-index facets $\{310\}$ on the Au NRs observed in this study was facilitated by the Ag ions [23,60] stemming from the addition of $AgNO_3$ to the seed-mediated solution. Stabilization of the facets $\{100\}$ is often attributed to the presence of bromide ions [29,62]. In our case, the bromide ions stem from the seeds that were synthesized using the CTAB protocol [24,40].

In literature, Au NRs with alternating high-index $\{310\}$ and low-index $\{100\}$ facets bordering their cross sections are reported more frequently than the Au NRs terminated exclusively by the high-index facets [63–65]. Also in our sample, $\sim$ 43% of the Au NRs were terminated by mixed high-index and low-index facets. An analogous result was also obtained for the NR caps, which were predominantly *symmetric* (Figure 5). This result is in a good agreement with previous investigations [23,24,66,67] showing that, under uninhibited growth conditions, the *symmetric* caps occur more frequently than the *asymmetric* caps. The *symmetric* or *asymmetric* arrangement of the NR caps can, however, depend on the aspect ratio of the NRs. Ye *et al.* [24] reported that the amount of NRs with *asymmetric* caps increases, when the aspect ratio of the NRs increases.

3.3. Hierarchical Architecture of Multi-Core Iron Oxide Nanoparticles

In both previous examples, individual nanoparticles and nanorods were sufficiently separated from each other. Thus, they could be identified and quantified quite straightforwardly from the HAADF-STEM images using a shape-based segmentation routine [40]. However, this routine fails, when it is applied to overlying objects, *e.g.*, to multi-core iron oxide nanoparticles (IONPs). An example of a multi-core IONP is shown in Figure 6a. The multi-core nature of the IONP becomes clearly visible from the FFTs of the HRTEM images (Figures 6b and 6c), which disclose different orientations of the cores A and B along the direction of the primary electron beam, *i.e.*, $[\bar{1}12]_A$ and $[\bar{2}17]_B$.

 doi:10.20944/preprints202409.0256.v1

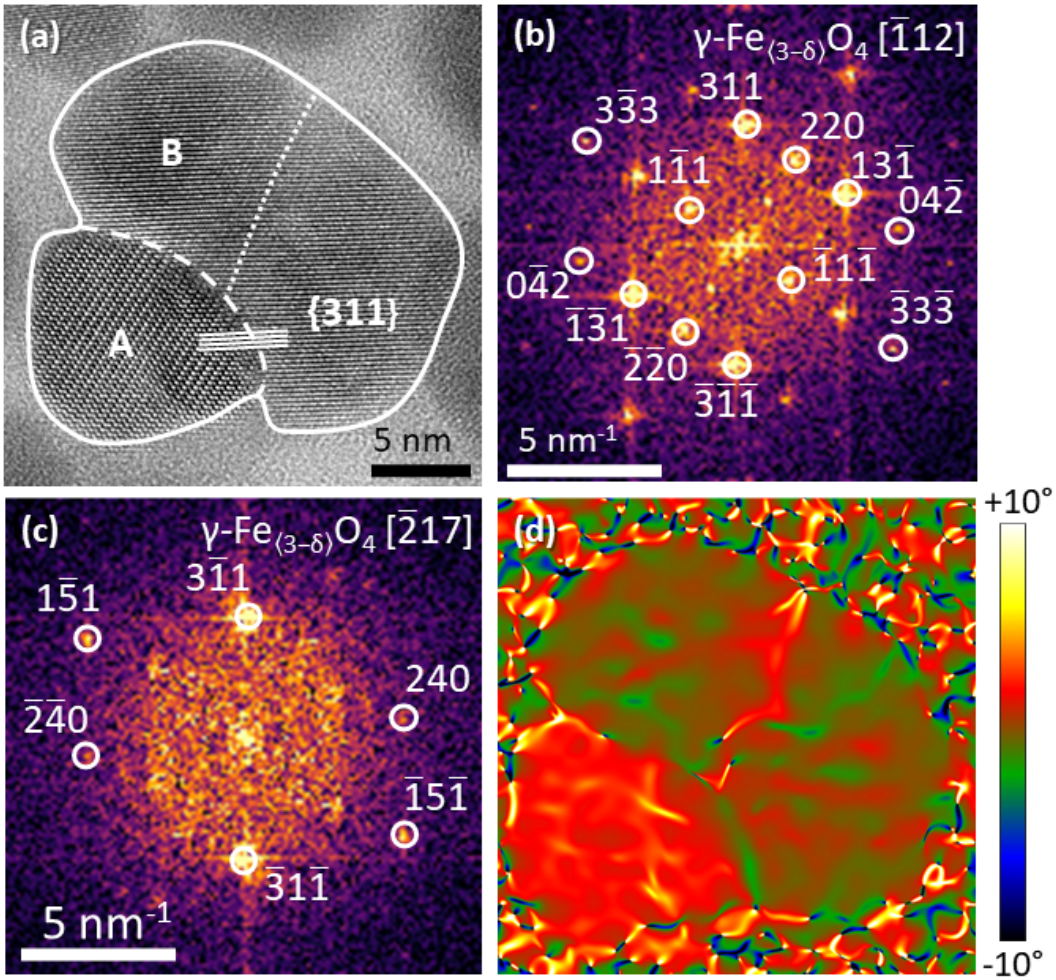

Figure 6. (a) HRTEM image of an iron oxide nanoparticle (Fe_3O_4, magnetite, space group $Fd\bar{3}m$) that consists of two cores, A and B. The outline of the NP and the interface between the two cores are highlighted by the solid line and by the dashed line, respectively. The dotted line marks a low-angle boundary between two nanocrystals having almost the same orientation. (b) and (c) Local FFTs of the HRTEM regions corresponding to the cores A and B. (d) Rigid rotation field determined by geometric phase analysis [38,39].

The attachment of differently oriented cores is facilitated by the agreement in the distances of the parallel lattice planes of both counterparts at their interface. In the mutual orientation relationship of the cores from Figure 6a, the following lattice planes are almost parallel and their interplanar distances equal: $(311)_A \parallel (3\bar{1}1)_B$, $(3\bar{3}3)_A \parallel (1\bar{5}1)_B$ and $(0\bar{4}2)_A \parallel (\bar{2}\bar{4}0)_B$, s. Figures 6b and 6c. Slight differences in the local orientations within the cores are visible from the rigid rotation field (Figure 6d) that was determined using the geometric phase analysis (GPA) [38,39]. For GPA, the reflections 311_A, $3\bar{3}3_A$, $3\bar{1}1_B$ and $1\bar{5}1_B$ were used. While the GPA done on the core A did not reveal noticeable orientation variations, the GPA carried out on the core B indicated that this core consists possibly of two parts, which are separated by a low-angle boundary (dotted line in Figure 6a). These characteristics of the multi-core IONPs obtained from HRTEM and FFT/HRTEM, in particular the detailed information about the crystallographically oriented attachment of individual cores, are extremely helpful for understanding the formation of multi-core IONPs and their magnetic properties.

The multi-core IONPs show superparamagnetic behavior with a high saturation magnetization and a good biocompatibility, which makes them to favored materials for applications in biomedicine, especially in magnetic hyperthermia. The magnetic properties of the multi-core IONPs depend mainly

 doi:10.20944/preprints202409.0256.v1

on their size and chemical composition [8], but they are also affected by the disorder of the magnetic moments [68–70] and/or by the magnetic coupling between the neighboring cores [71]. Bulk iron ferrites are strongly ferrimagnetic, and exhibit spontaneous magnetic moment and hysteresis [72]. When the size of the IONPs is reduced, they become superparamagnetic [8] with nearly zero remanent magnetization and coercivity, but retain a high magnetic susceptibility. A further decrease of the IONP size leads to a decrease of the saturation magnetization of the IONPs, which is attributed to the magnetic disorder in the surface layer [73,74]. Another reason for the reduction of the saturation magnetization of IONPs is the presence of vacancies on the cation sites in the crystal structure of $Fe_{3-\delta}O_4$, which also contributes to the disorder of the magnetic moments and thus to the decrease of the saturation magnetization [75,76]. While the saturation magnetization of vacancy-free magnetite (Fe_3O_4, SG $Fd\bar{3}m$) is 92.8 Am^2/kg [77], the saturation magnetization of maghemite ($Fe_{2.667}O_4$, SG $P4_332$ or $P4_12_12$ [78]) is only 74.3 Am^2/kg [77].

In order to be able to distinguish individual parts of the multi-core IONPs from each other, the shape-based segmentation routine [40] was extended (Figure 7). In the first step (Figures 7a and 7b), the size of individual multi-core IONPs and the corresponding size distribution were determined from the projected area as described in Section 3.1. In the second step (Figures 7c-g), the individual IONPs were separated into the individual cores, which were quantified analogously. This two-step segmentation and quantification procedure revealed the size distribution functions, which are depicted in Figure 8a. The distribution density was calculated according to

$$q_0(D) = \frac{N_i/N}{D_i^{\max} - D_i^{\min}}, \tag{16}$$

where N_i is the number of particles within the respective "size category", *i.e.*, having their diameter between $D_i^{\max}$ and $D_i^{\min}$. D in the argument of the distribution function is the mean value of $D_i^{\max}$ and $D_i^{\min}$. $N = \sum_i N_i$ is the total number of particles. The distribution functions from Figure 8a were compared to the distribution function of the magnetic particle size (Figure 8b), which was determined using the Langevin fit of the magnetization curve measured by alternating gradient magnetometry on an ensemble of IONPs (inset in Figure 8b) [71].

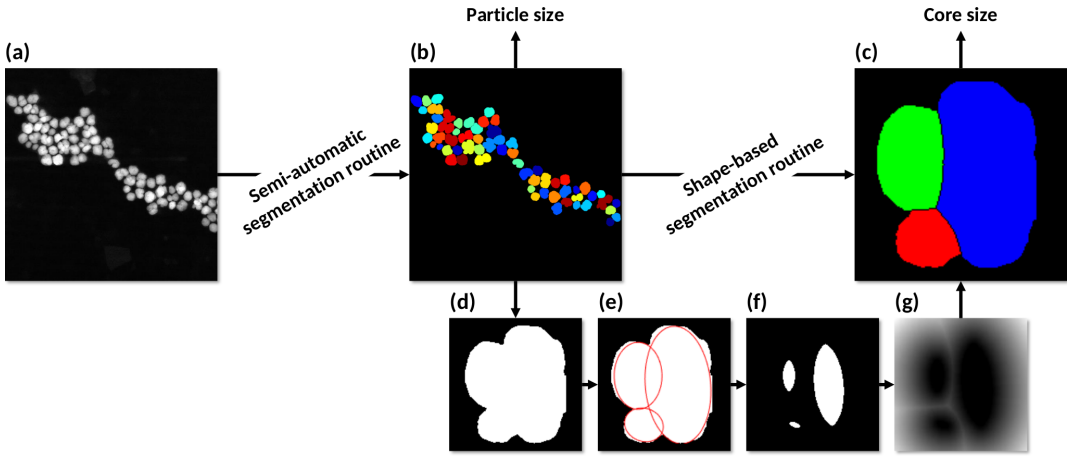

Figure 7. Schematic representation of the multi-stage segmentation routine used for determination of the particle size and core size distribution in multi-core IONPs. (a) Original low-magnification HAADF-STEM image of an ensemble of the multi-core IONPs. (b) HAADF-STEM image segmented by the semi-automatic segmentation routine [40] into individual multi-core IONPs. (c) Single multi-core IONP segmented into several cores by a shape-based segmentation routine complemented by the watershed [79] and DTECMA [80] algorithms. (d) Binary image of the multi-core IONP from panel (c). (e) The multi-core IONP split into individual elliptical cores using the DTECMA algorithm [80]. (f) Shape markers determined on the basis of the ellipses from panel (e). (g) The marker-controlled segmentation using the Euclidean distance transform and the watershed algorithm [81].

 doi:10.20944/preprints202409.0256.v1

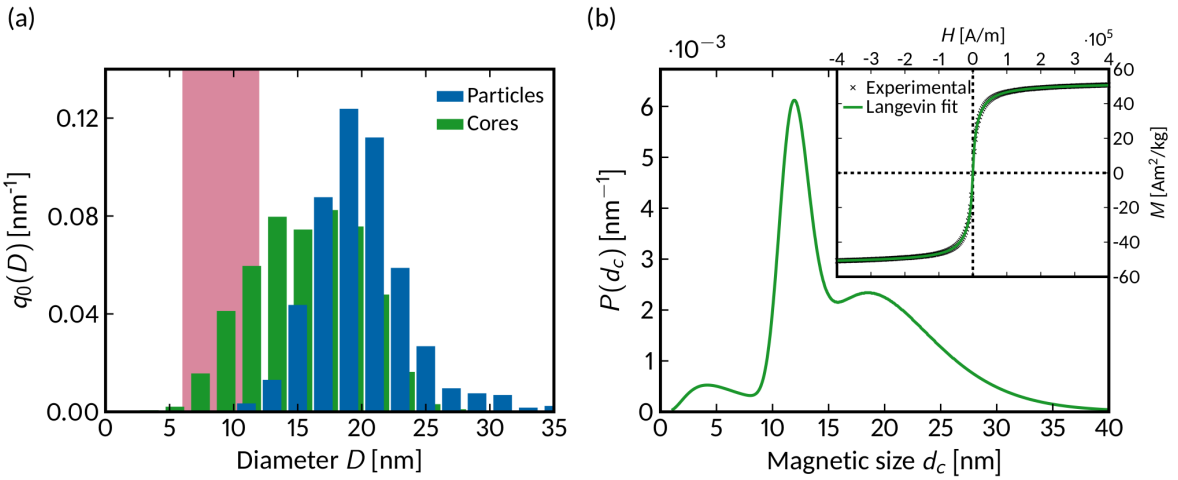

Figure 8. (a) Distribution density, $q_0(D)$, of the size of the multi-core IONPs (Particles) and their cores (Cores) as determined from the HAADF-STEM images. The broad red band marks the diameter range of the cores and core fragments (nanocrystals within the cores) that was obtained from the HRTEM images. (b) Distribution of the magnetic particle sizes as determined using the Langevin fit of the magnetization curve. The magnetization curve and its Langevin fit are shown in the inset.

In analogy with the model of the multi-core IONPs suggested on the basis of the HRTEM and HAADF-STEM results (Figures 6 and 7), the presence of three categories of magnetic particles was assumed, corresponding to (i) the fragments of the cores (nanocrystals within the cores that are frequently terminated by low-angle boundaries), (ii) the individual cores and (iii) the multi-core IONPs. Hence, the distribution of the magnetic particle size (Figure 8b) was composed of three log-normal functions:

$$P(d_c) = \sum_{i=1}^{3} w_i \frac{1}{\sqrt{2\pi}\sigma_i d_c} \exp\left[-\frac{(\ln d_c - \mu_i)^2}{2\sigma_i^2}\right] \tag{17}$$

In Equation (17), w_i is the fraction of the magnetic particles having the mean size μ_i; σ_i is the width of the respective log-normal function. This distribution function was used to calculate the magnetization curve [82,83]:

$$M(H) = M_S \int_0^\infty P(d_c)\mathcal{L}(\xi)\mathrm{d}d_c, \tag{18}$$

where

$$\mathcal{L}(H) = \coth(\xi) - 1/\xi \tag{19}$$

is the Langevin function, which argument,

$$\xi = \frac{M_S \pi d_c^3 H \mu_0}{6 k_B T}, \tag{20}$$

depends on the saturation magnetization (M_S), on the size of the magnetic particles (d_c), on the temperature (T), and on the strength of the external magnetic field (H). μ_0 is the permeability of vacuum, k_B the Boltzmann constant. The calculated magnetization curve was fitted to the measured one (inset in Figure 8b). The refineable parameters were the saturation magnetization (M_S), the fraction of the magnetic particles (w_i), the medians of the magnetic particle sizes (μ_i), and the widths of the log-normal functions (σ_i). The starting values of μ_i and σ_i were taken from the HRTEM and HAADF-STEM results (Figure 8a).

For multi-core IONPs, the size distribution functions from Figures 8a and 8b match quite good. Both techniques, *i.e.*, the HAADF-STEM imaging and the determination of the size of the superparamagnetic nanoparticles from the magnetization curve [82], revealed the same mean size of the multi-core IONPs and the same width of the size distribution, (20 ± 5) nm. This means that in

 doi:10.20944/preprints202409.0256.v1

multi-core IONPs, the magnetic moments in individual cores are highly coupled. Thus, such multi-core IONPs resemble large magnetic particles. The coupling of the magnetic moments in neighboring cores is apparently facilitated by their specific orientation relationships, as it was shown exemplarily in Figure 6.

Mean size of the individual cores obtained from the magnetization curve, (12 ± 1) nm, also agrees with the size of the cores determined by HAADF-STEM. In this context, it should be noted that the 'magnetic' size of the cores is typically smaller than their geometric size, because the magnetization of small particles is reduced by a disordered spin layer at their surface [74]. Still, the size distribution function obtained for the individual cores from the HAADF-STEM analysis (Figures 8a) is much broader (and thus less intense) than the size distribution function determined from the magnetization curve (Figures 8b). As the analysis of the HAADF-STEM images classified the IONPs according to their 2D morphology (projected area) only and as it was not complemented by the information about the crystallographic orientations of adjacent cores, it cannot distinguish between the cores with coupled and uncoupled magnetic moments. Consequently, the size distribution function obtained from the HAADF-STEM measurements includes also multi-core IONPs with elliptical projected shape that consist of magnetically uncoupled cores. Finally, the fitting of the magnetization curve confirmed presence of the core fragments. However, their fraction was very low, because the majority of the core fragments possessed distinct mutual orientation relationships that facilitated a coordinated arrangement of the magnetic moments.

4. Conclusions

In this contribution, the capabilities of a correlative multi-scale nanoparticle characterization technique using the combination of high-resolution and low-resolution transmission electron microscopy were illustrated by means of the quantitative classification of gold nanoplates, multiply twinned gold nanoparticles, gold nanorods and multi-core iron oxide nanoparticles. In this classification procedure, the high-resolution transmission electron microscopy complemented by the fast Fourier transformation of the HRTEM images provides information about the two-dimensional shape of the nanoparticles (determined from the projected area), about the crystallographic directions, *e.g.*, about the orientations of the surface facets or about the orientation relationships between neighboring particles, and about the kind of the crystal structure defects. The high-angle annular dark-field scanning transmission electron microscopy (HAADF-STEM) performed in a lower resolution mode provides statistically relevant information about the three-dimensional shape of the nanoparticles (determined from the projected area and from the intensity of the Rutherford scattering that is proportional to the nanoparticle thickness), which can be correlated with the crystallographic information obtained from the HRTEM measurements, if some features of the 3D shape can unambiguously be assigned to the crystallographic directions. However, the HAADF-STEM intensity depends not only on the thickness of the investigated objects but also on the atomic number of the involved elements. Therefore, the most examples of the three-dimensional nanoparticle classification presented in this contribution were restricted to the materials containing a single type of atoms.

Author Contributions: S.N.: conceptualization, methodology, software, formal analysis, investigation, validation, visualization, writing – original draft preparation; D.R.: conceptualization, methodology, writing – review and editing, supervision, project administration, funding acquisition. Both authors have read and agreed to the published version of the manuscript.

Funding: This research was funded by Deutsche Forschungsgemeinschaft (DFG) within the priority program SPP 2045 "Highly specific and multidimensional fractionation of fine particle systems with technical relevance", grant number 313858392.

Data Availability Statement: Dataset available on request from the authors.

Acknowledgments: The authors thank to Azita Rezvani, Prof. Doris Segets (University of Duisburg-Essen, Germany), Matthäus Barasinski, Prof. Georg Garnweitner (TU Braunschweig, Germany), Laura Kuger, Dr. Carsten-Rene Arlt, Prof. Matthias Franzreb (KIT, Eggenstein-Leopoldshafen, Germany), Christina Menter, Ahmed

Salaheldin Mahmoud (University of Erlangen-Nürnberg, Germany) for supplying us with the nanoparticles, and to Astrid Leuteritz for the TEM sample preparation.

Conflicts of Interest: The authors declare no conflicts of interest.

References

1. Talapin, D.V.; Lee, J.S.; Kovalenko, M.V.; Shevchenko, E.V. Prospects of Colloidal Nanocrystals for Electronic and Optoelectronic Applications. *Chem. Rev.* **2010**, *110*, 389–458. doi:10.1021/cr900137k.
2. Kovalenko, M.V.; Manna, L.; Cabot, A.; Hens, Z.; Talapin, D.V.; Kagan, C.R.; Klimov, V.I.; Rogach, A.L.; Reiss, P.; Milliron, D.J.; Guyot-Sionnnest, P.; Konstantatos, G.; Parak, W.J.; Hyeon, T.; Korgel, B.A.; Murray, C.B.; Heiss, W. Prospects of Nanoscience with Nanocrystals. *ACS Nano* **2015**, *9*, 1012–1057. doi:10.1021/nn506223h.
3. Chen, J.; Lim, B.; Lee, E.P.; Xia, Y. Shape-controlled synthesis of platinum nanocrystals for catalytic and electrocatalytic applications. *Nano Today* **2009**, *4*, 81–95. doi:10.1016/j.nantod.2008.09.002.
4. Zhou, K.; Li, Y. Catalysis based on nanocrystals with well-defined facets. *Angew. Chem. Int. Ed.* **2012**, *51*, 602–613. doi:10.1002/anie.201102619.
5. Dreaden, E.C.; Alkilany, A.M.; Huang, X.; Murphy, C.J.; El-Sayed, M.A. The golden age: gold nanoparticles for biomedicine. *Chem. Soc. Rev.* **2012**, *41*, 2740–2779. doi:10.1039/c1cs15237h.
6. Patra, J.K.; Das, G.; Fraceto, L.F.; Campos, E.V.R.; Rodriguez-Torres, M.D.P.; Acosta-Torres, L.S.; Diaz-Torres, L.A.; Grillo, R.; Swamy, M.K.; Sharma, S.; Habtemariam, S.; Shin, H.S. Nano based drug delivery systems: recent developments and future prospects. *J. Nanobiotechnology* **2018**, *16*, 71. doi:10.1186/s12951-018-0392-8.
7. Mayer, K.M.; Hafner, J.H. Localized surface plasmon resonance sensors. *Chem. Rev.* **2011**, *111*, 3828–3857. doi:10.1021/cr100313v.
8. Jeong, U.; Teng, X.; Wang, Y.; Yang, H.; Xia, Y. Superparamagnetic Colloids: Controlled Synthesis and Niche Applications. *Adv. Mater.* **2007**, *19*, 33–60. doi:10.1002/adma.200600674.
9. Smith, A.M.; Nie, S. Semiconductor Nanocrystals: Structure, Properties, and Band Gap Engineering. *Acc. Chem. Res.* **2010**, *43*, 190–200. doi:10.1021/ar9001069.
10. Guisbiers, G.; Mendoza-Cruz, R.; Bazán-Díaz, L.; Velázquez-Salazar, J.J.; Mendoza-Perez, R.; Robledo-Torres, J.A.; Rodriguez-Lopez, J.L.; Montejano-Carrizales, J.M.; Whetten, R.L.; José-Yacamán, M. Electrum, the Gold–Silver Alloy, from the Bulk Scale to the Nanoscale: Synthesis, Properties, and Segregation Rules. *ACS Nano* **2016**, *10*, 188–198. doi:10.1021/acsnano.5b05755.
11. Viswanatha, R.; Sarma, D.D. Effect of structural modification on the quantum-size effect in II-VI semiconducting nanocrystals. *Chem.: Asian J.* **2009**, *4*, 904–909. doi:10.1002/asia.200900046.
12. Tang, Y.; Ouyang, M. Tailoring properties and functionalities of metal nanoparticles through crystallinity engineering. *Nat. Mater.* **2007**, *6*, 754–759. doi:10.1038/nmat1982.
13. C. B. Murray and D. J. Norris and M. G. Bawendi. Synthesis and characterization of nearly monodisperse CdE (E = sulfur, selenium, tellurium) semiconductor nanocrystallites. *J. Am. Chem. Soc.* **1993**, *115*, 8706–8715. doi:10.1021/ja00072a025.
14. Burda, C.; Chen, X.; Narayanan, R.; El-Sayed, M.A. Chemistry and properties of nanocrystals of different shapes. *Chem. Rev.* **2005**, *105*, 1025–1102. doi:10.1021/cr030063a.
15. Zhang, Q.; Han, L.; Jing, H.; Blom, D.A.; Lin, Y.; Xin, H.L.; Wang, H. Facet Control of Gold Nanorods. *ACS Nano* **2016**, *10*, 2960–2974. doi:10.1021/acsnano.6b00258.
16. Slot, J.W.; Geuze, H.J. A new method of preparing gold probes for multiple-labeling cytochemistry. *Europ. J. Cell Biol.* **1985**, *38*, 87–93.
17. Shao, Y.; Jin, Y.; Dong, S. Synthesis of gold nanoplates by aspartate reduction of gold chloride. *Chem. Commun.* **2004**, pp. 1104–1105. doi:10.1039/B315732F.
18. Lofton, C.; Sigmund, W. Mechanisms Controlling Crystal Habits of Gold and Silver Colloids. *Advanced Functional Materials* **2005**, *15*, 1197–1208. doi:10.1002/adfm.200400091.
19. Park, J.; Joo, J.; Kwon, S.G.; Jang, Y.; Hyeon, T. Synthesis of monodisperse spherical nanocrystals. *Angew. Chem. Int. Ed.* **2007**, *46*, 4630–4660. doi:10.1002/anie.200603148.
20. Xia, Y.; Xiong, Y.; Lim, B.; Skrabalak, S. Shape-Controlled Synthesis of Metal Nanocrystals: Simple Chemistry Meets Complex Physics? *Angew. Chem. Int. Ed.* **2009**, *48*, 60–103. doi:10.1002/anie.200802248.
21. Zhang, Q.; Xie, J.; Yu, Y.; Yang, J.; Lee, J.Y. Tuning the Crystallinity of Au Nanoparticles. *Small* **2010**, *6*, 523–527. doi:10.1002/smll.200902033.

 doi:10.20944/preprints202409.0256.v1

22. Han, X.; Goebl, J.; Lu, Z.; Yin, Y. Role of Salt in the Spontaneous Assembly of Charged Gold Nanoparticles in Ethanol. *Langmuir* **2011**, *27*, 5282–5289. doi:10.1021/la200459t.
23. Personick, M.L.; Langille, M.R.; Zhang, J.; Mirkin, C.A. Shape Control of Gold Nanoparticles by Silver Underpotential Deposition. *Nano Lett.* **2011**, *11*, 3394–3398. doi:10.1021/nl201796s.
24. Ye, X.; Gao, Y.; Chen, J.; Reifsnyder, D.C.; Zheng, C.; Murray, C. Seeded Growth of Monodisperse Gold Nanorods Using Bromide-Free Surfactant Mixtures. *Nano Lett.* **2013**, *13*, 2163–2171. doi:10.1021/nl400653s.
25. Wang, Y.; Peng, H.C.; Liu, J.; Huang, C.Z.; Xia, Y. Use of Reduction Rate as a Quantitative Knob for Controlling the Twin Structure and Shape of Palladium Nanocrystals. *Nano Lett.* **2015**, *15*, 1445–1450. doi:10.1021/acs.nanolett.5b00158.
26. Salaheldin, A.M.; Walter, J.; Herre, P.; Levchuk, I.; Jabbari, Y.; Kolle, J.M.; Brabec, C.J.; Peukert, W.; Segets, D. Automated synthesis of quantum dot nanocrystals by hot injection: Mixing induced self-focusing. *J. Chem. Eng.* **2017**, *320*, 232–243. doi:10.1016/j.cej.2017.02.154.
27. Gavilán, H.; Kowalski, A.; Heinke, D.; Sugunan, A.; Sommertune, J.; Varón, M.; Bogart, L.K.; Posth, O.; Zeng, L.; González-Alonso, D.; Balceris, C.; Fock, J.; Wetterskog, E.; Frandsen, C.; Gehrke, N.; Grüttner, C.; Fornara, A.; Ludwig, F.; Veintemillas-Verdaguer, S.; Johansson, C.; Morales, M.P. Colloidal Flower-Shaped Iron Oxide Nanoparticles: Synthesis Strategies and Coatings. *Part. Part. Syst. Charact.* **2017**, *34*, 1700094. doi:10.1002/ppsc.201700094.
28. Walsh, M.J.; Tong, W.; Katz-Boon, H.; Mulvaney, P.; Etheridge, J.; Funston, A.M. A Mechanism for Symmetry Breaking and Shape Control in Single-Crystal Gold Nanorods. *Acc. Chem. Res.* **2017**, *50*, 2925–2935. doi:10.1021/acs.accounts.7b00313.
29. Park, J.E.; Lee, Y.; Nam, J.M. Precisely Shaped, Uniformly Formed Gold Nanocubes with Ultrahigh Reproducibility in Single-Particle Scattering and Surface-Enhanced Raman Scattering. *Nano Lett.* **2018**, *18*, 6475–6482. doi:10.1021/acs.nanolett.8b02973.
30. Mahmoud, A.S.; Segets, D. Cleaning Matters! *ACS Comb. Sci.* **2019**, *21*, 722–725. doi:10.1021/acscombsci.9b00122.
31. Yang, T.H.; Shi, Y.; Janssen, A.; Xia, Y. Surface Capping Agents and Their Roles in Shape-Controlled Synthesis of Colloidal Metal Nanocrystals. *Angew. Chem. Int. Ed.* **2020**, *59*, 15378–15401. doi:10.1002/anie.201911135.
32. Kumar, C.S., Ed. *UV-VIS and Photoluminescence Spectroscopy for Nanomaterials Characterization*; Springer Berlin Heidelberg: Berlin, Heidelberg, 2013.
33. Pecora, R. Dynamic Light Scattering Measurement of Nanometer Particles in Liquids. *Journal of Nanoparticle Research* **2000**, *2*, 123–131. doi:10.1023/A:1010067107182.
34. Ingham, B. X-ray scattering characterisation of nanoparticles. *Crystallography Reviews* **2015**, *21*, 229–303. doi:10.1080/0889311X.2015.1024114.
35. Furat, O.; Leißner, T.; Ditscherlein, R.; Šedivý, O.; Weber, M.; Bachmann, K.; Gutzmer, J.; Peuker, U.; Schmidt, V. Description of Ore Particles from X-Ray Microtomography (XMT) Images, Supported by Scanning Electron Microscope (SEM)-Based Image Analysis. *Microsc. Microanal.* **2018**, *24*, 461–470. doi:10.1017/S1431927618015076.
36. Furat, O.; Leißner, T.; Bachmann, K.; Gutzmer, J.; Peuker, U.; Schmidt, V. Stochastic Modeling of Multidimensional Particle Properties Using Parametric Copulas. *Microsc. Microanal.* **2019**, *25*, 720–734. doi:10.1017/S1431927619000321.
37. Ditscherlein, R.; Furat, O.; de Langlard, M.; Martins de Souza e Silva, J.; Sygusch, J.; Rudolph, M.; Leißner, T.; Schmidt, V.; Peuker, U.A. Multiscale Tomographic Analysis for Micron-Sized Particulate Samples. *Microsc. Microanal.* **2020**, *26*, 676–688. doi:10.1017/S1431927620001737.
38. Hÿtch, M.; Snoeck, E.; Kilaas, R. Quantitative measurement of displacement and strain fields from HREM micrographs. *Ultramicroscopy* **1998**, *74*, 131–146. doi:10.1016/S0304-3991(98)00035-7.
39. Hÿtch, M.; Putaux, J.L.; Pénisson, J.M. Measurement of the displacement field of dislocations to 0.03 Å by electron microscopy. *Nature* **2003**, *423*, 270–273. doi:10.1038/nature01638.
40. Neumann, S.; Rezvani, A.; Barasinski, M.; Garnweitner, G.; Segets, D.; Rafaja, D. Statistical Determination of Atomic-Scale Characteristics of Au Nanocrystals Based on Correlative Multiscale Transmission Electron Microscopy. *Microsc. Microanal.* **2022**, *29*, 118–130. doi:10.1093/micmic/ozac027.
41. Rezvani, A.; Li, Y.; Neumann, S.; Anwar, O.; Rafaja, D.; Reichenberger, S.; Segets, D. Stability of binary colloidal mixtures of Au noble metal and ZnS semiconductor nanoparticles. *Colloids and Surfaces A: Physicochemical and Engineering Aspects* **2024**, *682*, 132832. doi:10.1016/j.colsurfa.2023.132832.

42. Barasinski, M.; Hilbig, J.; Neumann, S.; Rafaja, D.; Garnweitner, G. Simple model of the electrophoretic migration of spherical and rod-shaped Au nanoparticles in gels with varied mesh sizes. *Colloids and Surfaces A: Physicochemical and Engineering Aspects* **2022**, *651*, 129716. doi:10.1016/j.colsurfa.2022.129716.
43. Bender, P.; Fock, J.; Frandsen, C.; Hansen, M.F.; Balceris, C.; Ludwig, F.; Posth, O.; Wetterskog, E.; Bogart, L.K.; Southern, P.; Szczerba, W.; Zeng, L.; Witte, K.; Grüttner, C.; Westphal, F.; Honecker, D.; González-Alonso, D.; Fernández Barquín, L.; Johansson, C. Relating Magnetic Properties and High Hyperthermia Performance of Iron Oxide Nanoflowers. *J. Phys. Chem. C* **2018**, *122*, 3068–3077. doi:10.1021/acs.jpcc.7b11255.
44. Lartigue, L.; Hugounenq, P.; Alloyeau, D.; Clarke, S.P.; Lévy, M.; Bacri, J.C.; Bazzi, R.; Brougham, D.F.; Wilhelm, C.; Gazeau, F. Cooperative Organization in Iron Oxide Multi-Core Nanoparticles Potentiates Their Efficiency as Heating Mediators and MRI Contrast Agents. *ACS Nano* **2012**, *6*, 10935–10949. doi:10.1021/nn304477s.
45. Daniel, M.C.; Astruc, D. Gold Nanoparticles: Assembly, Supramolecular Chemistry, Quantum Size Related Properties, and Applications toward Biology, Catalysis, and Nanotechnology. *Chem. Rev.* **2004**, *104*, 293–346. doi:10.1021/cr030698+.
46. Amendola, V.; Pilot, R.; Frasconi, M.; Maragò, O.M.; Iatì, M.A. Surface plasmon resonance in gold nanoparticles: a review. *Journal of Physics: Condensed Matter* **2017**, *29*, 203002. doi:10.1088/1361-648x/aa60f3.
47. Mie, G. Beiträge zur Optik trüber Medien, speziell kolloidaler Metallösungen. *Ann. Phys.* **1908**, *330*, 377–445. doi:10.1002/andp.19083300302.
48. Link, S.; El-Sayed, M.A. Size and Temperature Dependence of the Plasmon Absorption of Colloidal Gold Nanoparticles. *J. Phys. Chem. B* **1999**, *103*, 4212–4217. doi:10.1021/jp984796o.
49. Yang, P.; Portalès, H.; Pileni, M.P. Dependence of the localized surface plasmon resonance of noble metal quasispherical nanoparticles on their crystallinity-related morphologies. *J. Chem. Phys.* **2011**, *134*, 024507. doi:10.1063/1.3523645.
50. Barnard, A.S.; Young, N.P.; Kirkland, A.I.; van Huis, M.A.; Xu, H. Nanogold: A Quantitative Phase Map. *ACS Nano* **2009**, *3*, 1431–1436. doi:10.1021/nn900220k.
51. Reyes-Gasga, J.; Tehuacanero-Nuñez, S.; Montejano-Carrizales, J.M.; Gao, X.; Jose-Yacaman, M. Analysis of the contrast in icosahedral gold nanoparticles. *Top. Catal.* **2007**, *46*, 23–30. doi:10.1007/s11244-007-0311-y.
52. Nellist, P.D.; Pennycook, S.J. The principles and interpretation of annular dark-field Z-contrast imaging. In *Advances in Imaging and Electron Physics*; Kazan, B.; Mulvey, T.; Hawkes, P.W., Eds.; 2000; Vol. 113, pp. 147–203. doi:10.1016/S1076-5670(00)80013-0.
53. Silverman, B.W. *Density Estimation for Statistics and Data Analysis*; Chapman and Hall/CRC: Boca Raton, 1998.
54. Scott, D.W. *Multivariate Density Estimation: Theory, Practice, and Visualization*; John Wiley & Sons, Inc.: New York, 1992.
55. Flüeli, M.; Borel, J.P. Surface energy anisotropy measurements on a small cuboctahedron of gold observed by high resolution electron microscopy (HREM). *J. Cryst. Growth* **1988**, *91*, 67–70. doi:10.1016/0022-0248(88)90368-5.
56. Fleury, B.; Cortes-Huerto, R.; Taché, O.; Testard, F.; Menguy, N.; Spalla, O. Gold Nanoparticle Internal Structure and Symmetry Probed by Unified Small-Angle X-ray Scattering and X-ray Diffraction Coupled with Molecular Dynamics Analysis. *Nano Lett.* **2015**, *15*, 6088–6094. doi:10.1021/acs.nanolett.5b02924.
57. Kirkland, A.I.; Jefferson, D.A.; Duff, D.G.; Edwards, P.P.; Gameson, I.; Johnson, B.F.G.; Smith, D.J. Structural studies of trigonal lamellar particles of gold and silver. *Proc. Math. Phys. Eng. Sci.* **1993**, *440*, 589–609. doi:10.1098/rspa.1993.0035.
58. Xiong, Y.; Washio, I.; Chen, J.; Cai, H.; Li, Z.Y.; Xia, Y. Poly(vinyl pyrrolidone): A Dual Functional Reductant and Stabilizer for the Facile Synthesis of Noble Metal Nanoplates in Aqueous Solutions. *Langmuir* **2006**, *22*, 8563–8570. doi:10.1021/la061323x.
59. Zheng, J.; Cheng, X.; Zhang, H.; Bai, X.; Ai, R.; Shao, L.; Wang, J. Gold Nanorods: The Most Versatile Plasmonic Nanoparticles. *Chem. Rev.* **2021**, *121*, 13342–13453. doi:10.1021/acs.chemrev.1c00422.
60. Langille, M.R.; Personick, M.L.; Zhang, J.; Mirkin, C.A. Defining Rules for the Shape Evolution of Gold Nanoparticles. *J. Am. Chem. Soc.* **2012**, *134*, 14542–14554. doi:10.1021/ja305245g.
61. Lohse, S.E.; Burrows, N.D.; Scarabelli, L.; Liz-Marzán, L.M.; Murphy, C.J. Anisotropic Noble Metal Nanocrystal Growth: The Role of Halides. *Chem. Mater.* **2014**, *26*, 34–43. doi:10.1021/cm402384j.

62. Peng, H.C.; Xie, S.; Park, J.; Xia, X.; Xia, Y. Quantitative Analysis of the Coverage Density of Br-Ions on Pd{100} Facets and Its Role in Controlling the Shape of Pd Nanocrystals. *J. Am. Chem. Soc.* **2013**, *135*, 3780–3783. doi:10.1021/ja400301k.
63. Goris, B.; Bals, S.; van den Broek, W.; Carbó-Argibay, E.; Gómez-Graña, S.; Liz-Marzán, L.; van Tendeloo, G. Atomic-scale determination of surface facets in gold nanorods. *Nat. Mater.* **2012**, *11*, 930–935. doi:10.1038/nmat3462.
64. Katz-Boon, H.; Walsh, M.; Dwyer, C.; Mulvaney, P.; Funston, A.M.; Etheridge, J. Stability of Crystal Facets in Gold Nanorods. *Nano Lett.* **2015**, *15*, 1635–1641. doi:10.1021/acs.nanolett.5b00124.
65. Tong, W.; Katz-Boon, H.; Walsh, M.J.; Weyland, M.; Etheridge, J.; Funston, A.M. The evolution of size, shape, and surface morphology of gold nanorods. *Chem. Comm.* **2018**, *54*, 3022–3025. doi:10.1039/C7CC08336J.
66. Lu, F.; Zhang, Y.; Zhang, L.; Zhang, Y.; Wang, J.X.; Adzic, R.R.; Stach, E.A.; Gang, O. Truncated ditetragonal gold prisms as nanofacet activators of catalytic platinum. *J. Am. Chem. Soc.* **2011**, *133*, 18074–18077. doi:10.1021/ja207848e.
67. Qin, Y.; Pan, W.; Yu, D.; Lu, Y.; Wu, W.; Zhou, J. Stepwise evolution of Au micro/nanocrystals from an octahedron into a truncated ditetragonal prism. *Chem. Commun.* **2018**, *54*, 3411–3414. doi:10.1039/C8CC00973B.
68. Chen, J.P.; Sorensen, C.M.; Klabunde, K.J.; Hadjipanayis, G.C.; Devlin, E.; Kostikas, A. Size-dependent magnetic properties of $MnFe_2O_4$ fine particles synthesized by coprecipitation. *Phys. Rev. B* **1996**, *54*, 9288–9296. doi:10.1103/PhysRevB.54.9288.
69. Caruntu, D.; Caruntu, G.; O'Connor, C.J. Magnetic properties of variable-sized Fe_3O_4 nanoparticles synthesized from non-aqueous homogeneous solutions of polyols. *J. Phys. D: Appl. Phys.* **2007**, *40*, 5801–5809. doi:10.1088/0022-3727/40/19/001.
70. Millan, A.; Urtizberea, A.; Silva, N.; Palacio, F.; Amaral, V.; Snoeck, E.; Serin, V. Surface effects in maghemite nanoparticles. *J. Magn. Magn. Mater.* **2007**, *312*, L5–L9. doi:10.1016/j.jmmm.2006.09.011.
71. Neumann, S.; Kuger, L.; Arlt, C.R.; Franzreb, M.; Rafaja, D. Influence of the hierarchical architecture of multi-core iron oxide nanoflowers on their magnetic properties. *Scientific reports* **2023**, *13*, 5673. doi:10.1038/s41598-023-31294-4.
72. Hummel, R.E. *Electronic Properties of Materials*; Springer: New York, NY, 2011. doi:10.1007/978-1-4419-8164-6.
73. Morales, M.; Pecharroman, C.; Gonzalez Carreñ, T.; Serna, C. Structural Characteristics of Uniform γ-Fe_2O_3 Particles with Different Axial (Length/Width) Ratios. *Journal of Solid State Chemistry* **1994**, *108*, 158–163. doi:10.1006/jssc.1994.1024.
74. Morales, M.P.; Veintemillas-Verdaguer, S.; Montero, M.I.; Serna, C.J.; Roig, A.; Casas, L.; Martínez, B.; Sandiumenge, F. Surface and Internal Spin Canting in γ-Fe_2O_3 Nanoparticles. *Chemistry of Materials* **1999**, *11*, 3058–3064. doi:10.1021/cm991018f.
75. Filippousi, M.; Angelakeris, M.; Katsikini, M.; Paloura, E.; Efthimiopoulos, I.; Wang, Y.; Zamboulis, D.; Van Tendeloo, G. Surfactant Effects on the Structural and Magnetic Properties of Iron Oxide Nanoparticles. *The Journal of Physical Chemistry C* **2014**, *118*, 16209–16217. doi:10.1021/jp5037266.
76. Baaziz, W.; Pichon, B.P.; Fleutot, S.; Liu, Y.; Lefevre, C.; Greneche, J.M.; Toumi, M.; Mhiri, T.; Begin-Colin, S. Magnetic Iron Oxide Nanoparticles: Reproducible Tuning of the Size and Nanosized-Dependent Composition, Defects, and Spin Canting. *The Journal of Physical Chemistry C* **2014**, *118*, 3795–3810. doi:10.1021/jp411481p.
77. Dunlop, D.; Özdemir, O. *Rock Magnetism: Fundamentals and Frontiers*; Cambridge University Press: Cambridge, 1997. doi:10.1017/CBO9780511612794.
78. Shmakov, A.N.; Kryukova, G.N.; Tsybulya, S.V.; Chuvilin, A.L.; Solovyeva, L.P. Vacancy Ordering in γ-Fe_2O_3: Synchrotron X-ray Powder Diffraction and High-Resolution Electron Microscopy Studies. *J. Appl. Cryst.* **1995**, *28*, 141–145. doi:10.1107/S0021889894010113.
79. Meyer, F. Topographic distance and watershed lines. *Signal Processing* **1994**, *38*, 113–125. doi:10.1016/0165-1684(94)90060-4.
80. Zou, T.; Pan, T.; Taylor, M.; Stern, H. Recognition of overlapping elliptical objects in a binary image. *Pattern Anal. Appl.* **2021**, *24*, 1193–1206. doi:10.1007/s10044-020-00951-z.
81. Soille, P. *Morphological Image Analysis*; Springer: Berlin, Heidelberg, 2013. doi:10.1007/978-3-662-05088-0.
82. Chen, D.X.; Sanchez, A.; Taboada, E.; Roig, A.; Sun, N.; Gu, H.C. Size determination of superparamagnetic nanoparticles from magnetization curve. *J. Appl. Phys.* **2009**, *105*, 083924. doi:10.1063/1.3117512.

 doi:10.20944/preprints202409.0256.v1

83. Karpavičius, A.; Coene, A.; Bender, P.; Leliaert, J. Advanced analysis of magnetic nanoflower measurements to leverage their use in biomedicine. *Nanoscale Advances* **2021**, *3*, 1633–1645. doi:10.1039/D0NA00966K.